Article

Exploring Geometric Properties and Cycle Design in Packed Bed and Monolith Contactors Using Temperature-Vacuum Swing Adsorption Modeling for Direct Air Capture

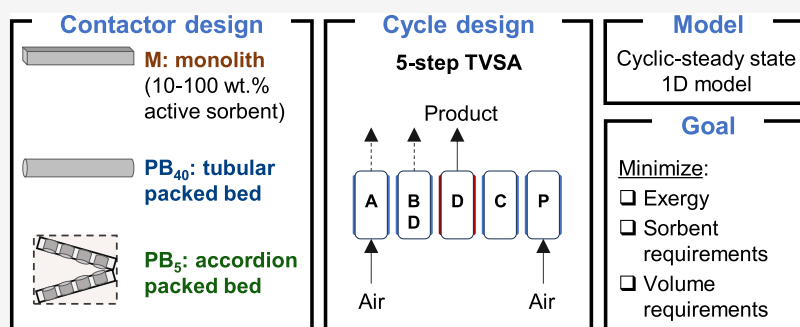Valentina Stampi-Bombelli and Marco Mazzotti*

Read Online

ACCESS | 📊 Metrics & More | 📰 Article Recommendations | 🆂🅸 Supporting Information

ABSTRACT: This study presents a comprehensive comparison between the packed bed and monolith contactor configurations for direct air capture (DAC) via process modeling of a temperature-vacuum swing adsorption (TVSA) process. We investigate various design parameters to optimize performance across different contactor geometries, including pellet size, monolith wall thickness, active sorbent content in monoliths, and packed bed structure configurations, considering both a traditional long column (PB_{40}) and multiple shorter columns configured in parallel (PB_5). Our parametric analysis assesses specific exergy consumption, sorbent, and volume requirements across different operating conditions of a five-step TVSA cycle. For minimizing sorbent requirements, PB_5 and monoliths with over 80% sorbent loading were the best-performing contactor designs with overlapping performance in the low-exergy region. Beyond this region, PB_5 faced limitations in reducing sorbent requirements further and was constrained by a maximum velocity at which it is sensible to operate without substantially increasing the exergy demand. In contrast, monoliths decreased sorbent requirements with minimal exergy increase due to reduced mass transfer resistances and lower pressure drop associated with their thin walls. The analysis of volume requirement-specific exergy Pareto fronts revealed that PB_5 was less competitive with this metric due to the requirements for additional void space in the contactor configuration. The study also revealed that optimal sorbent loading for reducing volume requirements in monoliths differed from those minimizing sorbent usage, with the most effective loading being below 100%. Thus, the optimal contactor design varies depending on the goals of minimizing sorbent and volume requirements, and the choice and design of the contactor will depend on the relative costs of these factors. Lastly, our findings challenge the assumption that higher velocities are always preferable for direct air capture, suggesting instead that the operating velocity depends on the contactor configuration.

1. INTRODUCTION

In alignment with the 2015 Paris Agreement, global efforts to limit warming to a 1.5 °C increase above preindustrial levels call for substantial reductions in CO_2 emissions.[1] Although decarbonizing mobility, households, industry, and power generation is crucial, these measures are slow to implement and incomplete, leaving residual emissions in so-called hard-to-abate sectors that need to be addressed. Thus, negative emission technologies (NETs) that allow for carbon dioxide removal (CDR) from the atmosphere, such as afforestation, bioenergy with carbon capture and storage, and direct air capture and carbon storage, play a vital role. Direct air capture (DAC), a technology that extracts CO_2 directly from the atmosphere,

emerges as a promising CDR technology. Employing both solid sorbents (adsorption) and liquid solvents (absorption), DAC research and deployment are brought forward by both academia and industry, with companies like Climeworks, Global Thermostat, and Carbon Engineering leading the way. The lower energy demand for sorbent regeneration in adsorption offers an

advantage over absorption (with heats of desorption of ca. 40−90 kJ/mol vs 200 kJ/mol in adsorption and absorption, respectively[2,3]), yet DAC's widespread adoption hinges on resolving significant technical and economic challenges.

The low concentration of CO_2 and the unavoidable humidity in the air are two of the primary challenges associated with DAC. As a result, a large portion of DAC research has centered around developing materials with high CO_2 capacity and selectivity over N_2 and O_2,[4,5] evaluating sorbent stability[4,6−8] and accurately characterizing CO_2−H_2O coadsorption.[9−13] Amine-functionalized materials have emerged as promising sorbents, offering high CO_2 capacities even in dilute CO_2 conditions, often enhanced in humid environments.[12,14,15] However, despite their favorable thermodynamic properties, amine-functionalized sorbents have been shown to exhibit kinetic limitations.[11,16−20] Various studies have shown that external and internal diffusion resistances in the gas phase are the limiting mechanisms defining the adsorption kinetics,[20−22] with their limitations increasing as the feed concentration decreases.[21,22] This is particularly relevant in DAC, where a low CO_2 concentration significantly affects gas-phase mass transport, contributing to slow kinetics, early breakthrough, and inefficient sorbent utilization. Experimental characterization of mass transfer kinetics under conditions relevant to DAC remains sparse despite its critical importance.[12,22,23] However, precise modeling of these dynamics is essential, as evidenced by the significant impact that the mass transfer coefficient, k, has on DAC performance through cyclic temperature-vacuum swing adsorption calculations.[24−26]

Another major challenge associated with the dilute CO_2 concentration in the feed is that large volumetric amounts of air need to be processed to capture a significant amount of CO_2. Coupled with the desire to operate at high air velocities to maintain short cycle times, this requirement might result in a large pressure drop across the air−solid contactor, thus increasing the energy demand of the blowers. Given that pressure drop increases with longer beds, lower bed porosities, and higher velocities,[27,28] it is intuitive to reduce bed lengths or to increase bed porosities to accommodate high air velocities. Multiple new contactor designs have been proposed to achieve the goal of reducing pressure drop while trying to maintain a compact structure. These include thin-layered packed beds arranged in compact geometries, such as radial bed contactors,[12,24−26,29−33] and structured sorbents like laminates[34] and monoliths,[2,21,23,30,31,35−40] which are compact and feature high porosities. Monoliths have gained particular attention due to their wide use in the catalyst industry and readiness at a technical level. With their parallel channel configuration, they have been shown not only to reduce pressure drop but also to enhance mass transfer kinetics in point-source CO_2 capture applications,[41−46] thereby also potentially addressing the kinetic limitations inherent in DAC. Both packed bed and monolith structures present distinct advantages and drawbacks for DAC applications, each influenced by current technological and commercial realities.[28] Monoliths, although beneficial for their lower pressure drops and higher mass transfer rates, are typically constrained by lower sorbent loadings, while at the same time, monoliths tailored for DAC are not readily commercially available. On the other hand, packed beds exhibit a higher pressure drop but benefit from high sorbent loadings and the availability of commercially viable pelletized sorbents like Lewatit VP OC 1065 for easier scalability.

The literature contains only a limited number of direct and quantitative analyses comparing the packed bed and monolith configurations. In the field of point-source CO_2 capture, Rezaei and Webley demonstrated that monoliths not only yield reduced pressure drop and faster kinetics but also enhanced cyclic productivity.[41] In a further study, Rezaei et al. showed via vacuum swing adsorption cycle modeling that longer cycle times favor packed bed geometries while short cycle times favor monolith geometries.[47] These studies, however, were confined to traditional packed bed column designs without considering innovative configurations that may positively affect the pressure drop. Additionally, they focused solely on point-source CO_2 capture, which has distinct requirements and limitations compared to direct air capture. To the best of our knowledge, a direct and quantitative comparison of the packed bed against monolith configurations, specifically within the context of DAC, has not yet been done.

With the goal of performing a detailed comparison of packed bed and monolith contactors in DAC-relevant conditions, in previous works, we presented two novel adsorbents:[22,48] triamine-functionalized γ-alumina pellets and triamine-functionalized γ-alumina-coated mullite monoliths, with γ-alumina comprising 6.9 wt % of the total monolith mass. We collected CO_2 isotherm data[48] for these materials and conducted breakthrough experiments at 400 ppm dry CO_2, applying a 1D adsorption model to estimate mass transfer coefficients, which were validated against well-established literature correlations.[22] The monolith exhibited larger mass transfer coefficients during adsorption due to its lower CO_2 adsorption capacity and smaller sorbent size, notably the reduced wall thickness compared to the pellet diameter (0.4 mm vs 3 mm). The sorbent size proved to be a critical factor in our investigation, significantly affecting both mass transfer and pressure drop. Although the monolith demonstrated better performance during the adsorption step, the analysis did not include desorption. This research aims to provide a direct and novel comparative analysis of packed bed and monolith contactor geometries in the context of direct air capture via temperature-vacuum swing adsorption (TVSA) cycle modeling. The active sorbent used, triamine-grafted γ-alumina (referred to herein as TRI-al), has been selected based on the collected experimental thermodynamic and kinetic data from prior works.[22] We explore several geometric characteristics crucial to each contactor type as identified in the existing literature. These include (1) the pellet diameter and monolith wall thickness, (2) the active sorbent loading in monolith contactors, and (3) the configuration of the packed beds, exploring both a conventional column design and one that decreases pressure drop. To evaluate and compare the contactors under consideration, we perform an extensive sensitivity analysis on the operating parameters of a five-step TVSA DAC cycle, including feed velocity, adsorption step time, and desorption step time, and compute sorbent, volume, and energy demand.

While our study aims to advance the understanding of packed bed and monolith configurations for DAC cycles, we acknowledge that many aspects of DAC technology still require further investigation. The approach adopted in this work is deliberately grounded in the availability of characterized experimental data for sorbents in both pellet and monolith forms, ensuring a consistent comparison and aiming to minimize speculative assumptions. This research aims to provide a solid framework for evaluating packed bed and monolith systems based on current knowledge and experimentally validated parameters.
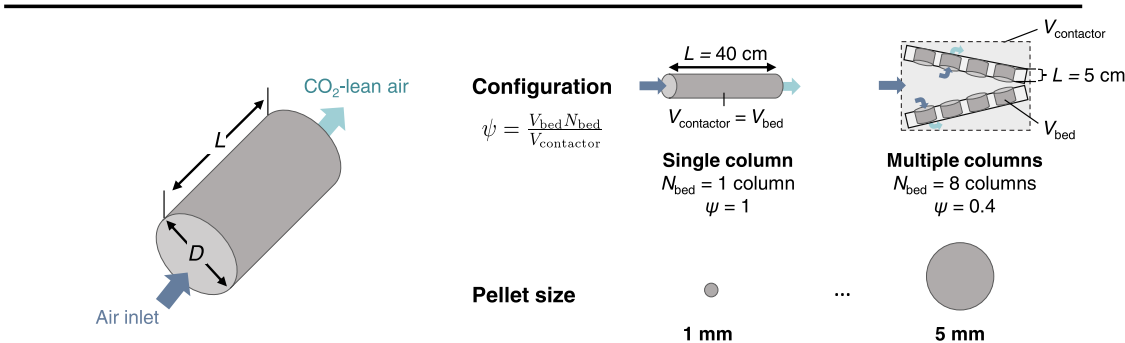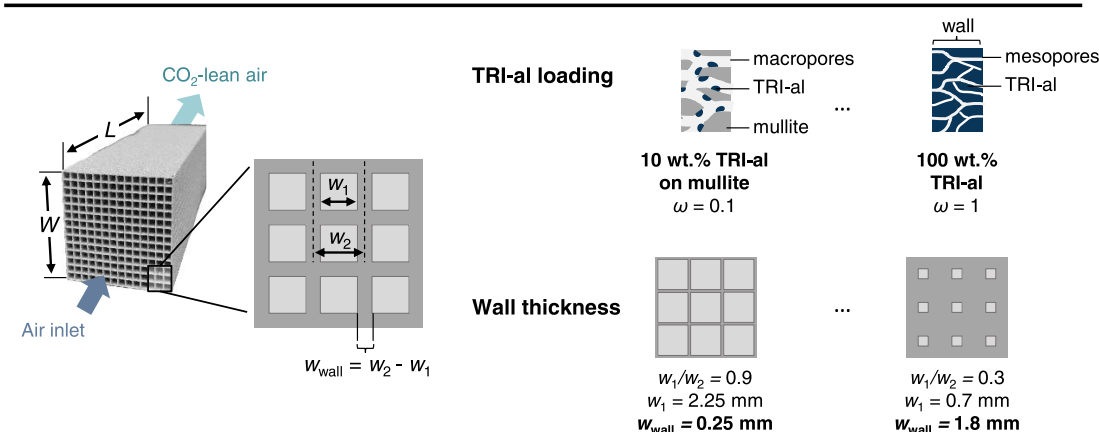
Figure 1. Visual illustration of the geometries of the packed bed and monolith contactors used in this work, along with the representation of the varied geometric characteristics: pellet size/wall thickness, packed bed configuration, and monolith TRI-al loading.

Table 1. Contactor Geometries Examined in this Study and Their Variation in Geometric Characteristics

acronym	type	sorbent size	TRI-al content	configuration
PB_{40} - PB_5	packed bed	d_p = 1−5 mm	ω = 1	single- and multicolumn
M^{10} - M^{100}	monolith	w_{wall} = 0.25−1.8 mm	ω = 0.1−1	single-column

2. METHODOLOGY

2.1. Materials and Contactor Geometries. *2.1.1. Active Sorbent Material.* The active sorbent material considered in this study is triamine-grafted γ-alumina (TRI-al), which was produced and experimentally characterized in prior works.[22,48] Details on sorbent synthesis and properties are reported in the Supporting Information (Section S1). Pure-component CO_2 and N_2 adsorption isotherms on TRI-al have been measured and published in prior works, demonstrating negligible N_2 adsorption and a favorable CO_2 isotherm.[22,48] A temperature-dependent Toth model was found to be well-suited to estimate CO_2 adsorption on TRI-al (eqs (S1) to (S4)), and the fitted Toth parameters and the heat of adsorption are provided in Table S1.[48] Mass transfer kinetics were characterized from breakthrough experiments and were compared with literature correlations that are further used in this study.[22]

2.1.2. Contactor Properties. This study employs two distinct sorbent geometries: spherical pellets consisting entirely of TRI-al and TRI-al-coated mullite honeycomb monoliths. Mullite is a macroporous material that provides the support structure of the monolith and adsorbs neither CO_2 nor N_2.[48] The TRI-al coat forms small pockets within the mullite macropores,[48] as shown in Figure 1, rather than a homogeneous layer on the mullite wall

like in the case of other sorbent-coated monoliths.[2,23] The monolith features a square cross-section, i.e., 3.5 cm in width and 40 cm in length. For modeling purposes, the monolith is represented as a cylindrical monolith with an equivalent cross-sectional area (D = 4 cm) to have the same gas velocity.[22] The pellets are arranged in a cylindrical packed bed column, measuring 4 cm in diameter and with different column lengths, as discussed below. Details of the material and contactor properties are provided in Table S2 for the packed bed and in Table S3 for the monolith.

2.1.3. Geometric Characteristics. While the materials that have been used and characterized in experiments consisted of one pellet size and one type of monolith with a given amount of TRI-al coating and a given wall thickness, in this work, we expand upon the previous experimental analyses to include additional geometric characteristics for two contactors whose DAC performance can be evaluated via modeling. In particular, we study the effect of (i) the sorbent size (pellet diameter or monolith wall thickness), (ii) the amount of TRI-al coating on the monolith, and (iii) the packed bed configuration. The contactors and their geometric characteristics are reported in Table 1 and illustrated in Figure 1.

2.1.3.1. Sorbent Size. The sorbent size, specifically the pellet diameter in packed beds and the wall thickness in monoliths, is the characteristic length that impacts mass transfer rates and pressure drops, as discussed quantitatively in Section 2.4. Monolith contactors are generally designed with wall thicknesses that are thinner than the typical pellet diameters found in packed beds; this decrease in characteristic diffusion length can substantially influence separation performance.[22,28,41] To quantify these differences using a TVSA model, we explore the effect of the characteristic length within the practical limits of each contactor. For the packed bed, we vary the pellet diameter within the feasible range of 1−5 mm to emulate industrially relevant sorbents while fulfilling particle diameter-to-bed diameter requirements (to avoid wall effects).[49] For the monoliths, we use a cell per square inch (CPSI) value of around 100, using a 14 × 14 cell structure with an overall cell width of w_2 = 2.5 mm. Then, we vary the channel width w_1 to achieve aspect ratio values, w_1/w_2, in the range 0.3−0.9, with 0.3 representing a very dense monolith with thick walls and narrow channels (w_{wall} = 1.8 mm) and 0.9 being a very porous monolith with thin walls and broad channels (w_{wall} = 0.25 mm). Here, the feasible lower wall thickness limit was set to 0.25 mm, which appears consistent with other works on honeycomb monoliths.[2,35,42]

2.1.3.2. Monolith TRI-al Coating. The second geometric characteristic concerns TRI-al loading in monoliths, denoted as ω, defining the ratio of active sorbent mass to total monolith mass, where the latter comprises both active sorbent (TRI-al) and inert support material (mullite). The TRI-al loading affects many aspects of a monolith, including its overall CO_2 capacity, the pore structure of the monolith walls, mass transfer kinetics, and the parasitic heat losses associated with heating up the inert support material during regeneration. We explore monoliths consisting of a TRI-al coating, varying between 10 and 90 wt % (ω = 0.1−0.9), on macroporous mullite substrates. Additionally, we explore the hypothetical case of monoliths made entirely of TRI-al (100 wt %, ω = 1), i.e., exploiting the maximum adsorption capacity of the monolith structure.

2.1.3.3. Packed Bed Configuration. The third geometric characteristic examined pertains to the packed bed configuration, whereby we explore two alternatives. The first is a conventional packed bed column, measuring 40 cm in length and 4 cm in diameter, identical to the dimensions of the monolith column. The second configuration, inspired by Climeworks' patents[33] and by the literature,[25,29] involves using the same amount of sorbent material in multiple shorter packed beds arranged in parallel to alleviate pressure drop. We assume a uniform flow distribution across the plate supporting the packed beds, ensuring equivalent velocities for all packed beds. For this configuration, we consider a contactor comprised of eight packed beds measuring 4 cm in diameter and 5 cm in length (see Figure 1). Unlike the single-column contactor, the total contactor volume must accommodate the extra void space necessary to realize this configuration. Here, we adopt a bed volume-to-contactor volume ratio of ψ = 0.4, as proposed in the literature,[25] implying that the combined volume of the eight packed bed columns occupies only 40% of the total contactor volume. Optimizing such a parameter and assessing its impact on separation performance is beyond the scope of this work.

Aspects pertinent to adsorption modeling, which vary with the geometric characteristics under investigation, such as bed density and porosities, are summarized in Tables S2 and S3 of the Supporting Information. Throughout the remainder of this work, all contactors under investigation will be referred to as C_L^ω,

where C indicates the contactor type (PB or M for packed bed and monolith, respectively), ω represents the weight percentage of active sorbent comprising the total solid weight, and L indicates the length. Given that all monoliths are 40 cm long and the packed beds contain 100% active sorbent material, for the sake of simplicity, they will be referred to simply as PB_L and M^ω for the rest of this work.

2.2. Cycle Design. The TVSA cycle analyzed in this study and shown in Figure 2 consists of five steps, namely, (1)
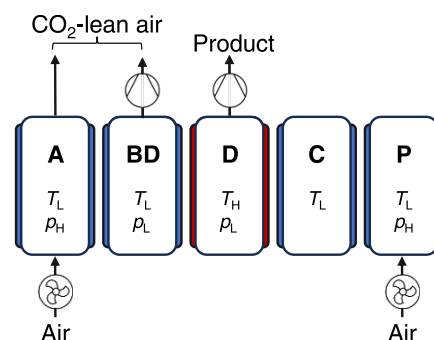
Figure 2. Five-step temperature-vacuum swing adsorption cycle used for the packed bed and monolith simulations. A: adsorption, BD: blowdown, D: desorption, C: cooling, and P: pressurization.

adsorption, (2) blowdown, (3) desorption, (4) cooling, and (5) pressurization. During the adsorption step, air at T_L = 25 °C is blown through the column with a blower, regulated by a back pressure regulator at the exit, and set at p_H = 1 bar, thus simulating ambient conditions. Our simulations are based on in-house adsorbents with characterized single-component CO_2 thermodynamic and kinetic properties. Due to the absence of binary CO_2−H_2O adsorption data for these materials, we conducted our simulations under the assumption of dry air. Due to the inert nature of N_2 and O_2 on this material,[22] dry air is modeled as a binary mixture of 400 ppm of CO_2 in 99.96% inert gas. Thus, in the adsorption step, CO_2 selectively adsorbs on the sorbent and the CO_2-lean air leaves the column. During the blowdown step, the column inlet is closed, and the column is evacuated to a vacuum pressure (p_L) for desorption. The discharged gas is released into the atmosphere, ensuring high CO_2 purity (>99%[50,51]) in the product by expelling the majority of the inert gas that is in the contactor voids at the end of adsorption. The desorption step involves heating the column to the desired regeneration temperature with the heat jacket while under a vacuum, enabling a combined pressure- and temperature-driven CO_2 desorption. The gas leaving the column during regeneration is collected in the product stream, which contains extracted CO_2 and must, therefore, be of high purity. Desorption is carried out at T_H = 100 °C and p_L = 10 mbar. While the desorption temperature of 100 °C permits the use of low-grade heat for heating, the vacuum pressure of 10 mbar remains notably low for industrial applications. As CO_2 is the only species desorbing during regeneration, its molar fraction can rapidly reach 1, with its partial pressure matching the vacuum level. Thus it is necessary to choose a vacuum pressure that allows operating with a positive value of the maximum cyclic capacity, defined as the difference between the equilibrium CO_2 loading under adsorption and desorption conditions. The isolines of maximum cyclic capacity, plotted in Figure S1, illustrate how the required regeneration pressure needs to be well below 100 mbar for feed temperatures between 10 and 30

°C. Thus, despite selecting a feed temperature of 25 °C for our simulations or even lower, it is obviously not possible to increase much regeneration pressures on TRI-al. After regeneration, the column is sealed and cooled to at least 70 °C to prevent the degradation of amines in the presence of oxygen.[52] Cooling times (t_C) of 450 s for the packed bed configurations and 950 s for the monolith configurations were sufficient to ensure that the entire column temperature dropped to 70 °C or below in all simulations. Finally, during the fifth process phase, the column is pressurized to atmospheric pressure (p_H) with air; then, the column is ready to start the cycle once again. In Table 2, a detailed overview of the fixed process parameters for each cycle step, including the duration, pressures, and external jacket temperatures, is provided.

Table 2. Process Conditions of the TVSA Cycles Analyzed in This Work, Including Constant Parameters and Lower and Upper Bounds of the Three Decision Variables: Adsorption Step Time (t_A), Adsorption Feed Flow Rate ($\dot{n}_{in}$), Desorption Step Time (t_D)

feed conditions		
y_{CO_2}	[−]	400 ppm
y_{air}	[−]	0.9996
T_{in}	[K]	298
flow rate	[mol s^{-1}]	0.002−0.12
Column Conditions		
p_H	[bar]	1
p_L	[bar]	0.01
T_H	[K]	373
T_L	[K]	298
Step Times		
t_A	[s]	700−200,000
t_{BD}	[s]	50
t_D	[s]	1000−20,000
t_C, monolith	[s]	950
t_C, packed bed	[s]	450
t_P	[s]	50

2.3. Mathematical Model. The model used to simulate the TVSA cycle is a first-principles model of a transient, one-dimensional cylindrical column of length L, consisting of material and energy balances involving the gas phase, the solid phase, and the column wall. The material and energy balances form a set of partial differential equations that are solved iteratively until a cyclic steady state is reached. The following assumptions are made:

- One-dimensional model in the axial direction with no radial concentration, temperature, or velocity gradients.
- The solid and gas phases are in thermal equilibrium with each other.
- The gas is described with the ideal gas law.
- The solid mass balance is written using the linear driving force (LDF) model in the solid phase with a lumped overall mass transfer coefficient k, which is kept constant within each step of the cycle:

$$\frac{\partial q}{\partial t} = k(q^* - q) \tag{1}$$

- Thermal conductivity in the axial direction is neglected.
- The heat capacities, the viscosity, the isosteric heat of adsorption, and the heat transfer coefficients are constant.

The detailed set of partial differential equations corresponding to the material and energy balances is reported in Table S4 of the Supporting Information (eqs (S5) to (S11)). The equations involved in the packed bed model and the monolith model differ only in the momentum balance, which is described by the Ergun equation for the packed bed and by the Hagen−Poiseuille equation for the monolith, as to eqs (S10) and (S11), respectively.

The CO_2 adsorption equilibrium is modeled using the temperature-dependent Toth isotherm, as given by eqs (S1) to (S4), with the corresponding parameters reported in Table S1. The presented model has been previously validated on a variety of cycle designs and applications for packed bed configurations.[53−55] Recently, validation efforts have been extended to include both packed bed and monolith contactor geometries through fixed bed DAC experiments utilizing the pellets and monolith sorbents described in Section S1.[22] More details on the model, its boundary conditions, and other applications can be found in previous works.[32,53]

2.4. Transport Phenomena. To accurately characterize the dynamics of each cycle step, we draw upon insights obtained from prior fixed bed breakthrough experiments conducted on both packed bed and monolith configurations with the materials presented in Section S1.[22] The model outlined in Table S4 was used to estimate transport parameters on these contactors, namely, the overall mass transfer coefficient, the axial dispersion coefficient, and the heat transfer coefficients between column, wall, and ambient surroundings. The values and correlations used to compute axial dispersion and heat transfer are summarized in Tables S2 and S3 and Table S5 (eqs (S12) to (S23)), respectively, while the determination of the overall mass transfer coefficient is discussed below.

The overall mass transfer coefficient, k, used in eq 1, is defined considering three resistances in series, as follows[56−59]

$$k(c, u, \text{geom.})$$
$$= \left[\frac{1}{k_f(u, \text{geom.})} \frac{q_V^*}{c} + \frac{1}{k_p(\text{geom.})} \frac{q_V^*}{c} + \frac{1}{k_s} \right]^{-1} \tag{2}$$

where k_f, k_p, and k_s are the film, gas pore, and solid mass transfer coefficients, respectively. Note that the adsorbed-phase concentration, q_V, is expressed in mol m$_{particle}^{-3}$, thus considering the volume occupied by sorbent and support, including its pores, but excluding the interparticle voids. In prior works, the estimation of individual mass transfer coefficients from break-through experiments[22] demonstrated close alignment with the established literature correlations, summarized in Table S5. Therefore, in the TVSA simulations presented in this study, these correlations will be employed to estimate k_f, k_p, and k_s for both the packed bed and the monolith.

The expression presented in eq 2 represents an extension of the Glueckauf approximation, which, in addition to its validity for linear isothermal systems, has demonstrated reasonable accuracy for nonlinear systems as well.[22,53,60] The quantity q_V^* is the adsorbed-phase concentration in equilibrium with the gas-phase concentration c, and the ratio q_V^*/c accounts for the effect of concentration on mass transfer in the case of nonlinear adsorption isotherms (note that in the case of a linear isotherm, this ratio coincides with the Henry's constant). As to the term q_V^*/c, often it has either been neglected in adsorption modeling (when k is estimated from literature correlations) or it has been assumed to be the same in all steps of the DAC cycle (when k is

either estimated from literature correlations or breakthrough experiments).[2,12,24−26,32,37] However, q_V^*/c can significantly affect the value of k as a consequence of the changes in the gas-phase concentration throughout the cycle. This is especially relevant in the case of DAC, where the very low CO_2 concentration in the feed results in notably lower mass transfer coefficients during adsorption compared to during desorption.[61] To account for the variation of q_V^*/c throughout the cycle while avoiding adding numerical complexities associated with updating its value at each time step and each location in the column during the simulation, q_V^*/c was determined for each of the five steps of the cycle at the beginning of the step and maintained constant during that step. For the adsorption and pressurization steps, we used the equilibrium ratio at the feed conditions $q_{V,in}^*/c_{in}$, an approach often adopted in the literature.[56−58,62] However, we have not found in the literature examples of the application of this approach to the blowdown, desorption, and cooling steps. Therefore, for these steps, we have decided to consider the CO_2 concentration at the temperature and pressure specified by the step's boundary conditions (T_L or T_H; p_L or p_H), assuming $y_{CO_2} = 1$, thus pretending that CO_2 is the only gas desorbing (see Section 2.2). While the assumption that the gas phase contains only CO_2 during the blowdown step is inaccurate as both CO_2 and the inert gas are removed from the interparticle voids, the step is so fast that no significant desorption of CO_2 from the solid phase occurs; thus, a precise estimation of k is less critical in this stage.

2.5. Key Performance Indicators. The metrics chosen to measure the performance of the DAC cycle in this study include CO_2 purity of the product stream, specific energy demand, and sorbent and volume requirements.

The purity of the extracted CO_2 is defined as follows

$$\Phi = \frac{N_{CO_2}}{N_{CO_2} + N_{inert}} \tag{3}$$

where N_{CO_2} and N_{inert} are the total number of moles of CO_2 and inert gas in the product stream, respectively.

Sorbent and volume requirements enable comparisons among DAC configurations that utilize different materials, contactors, and cycle designs. They measure the required sorbent mass and total volume to produce a specified amount of CO_2 per unit time

$$\hat{S} = \frac{m_{adsorbent}}{m_{CO_2}/t_{cycle}} \tag{4}$$

$$\hat{V} = \frac{V_{bed}}{m_{CO_2}/t_{cycle}} \tag{5}$$

where $m_{CO_2} = N_{CO_2} \times MW_{CO_2}$ is the mass of CO_2 in the product stream, t_{cycle} is the total cycle time, $m_{adsorbent}$ is the total adsorbent mass (including the mullite support in the case of TRI-al-coated monoliths), V_{bed} is the total contactor volume. The two metrics are related through $\hat{S} = \rho_b \psi \hat{V}$, where ρ_b is the bed density. Note that these metrics are the inverses of the mass and volumetric productivity metrics typically used in TVSA modeling. Note also that while the volume requirement is clearly a proxy for capital costs (it is controlled by the volume of the vessels that contain the adsorbent material), the sorbent requirement also contributes to the operating costs when the lifetime of the adsorbent is factored in (this is on the order of months to a few years, whereas the plant itself has a lifetime of decades).

The specific energy demand is an indicator of the operating costs of the DAC plant, accounting for both thermal (Q) and electrical (W) energy requirements. To ensure a consistent and fair comparison, these energy forms are expressed in terms of specific exergy (E_{spec}), which accounts for both energy quantity and energy quality. Electricity is pure exergy, while thermal energy needs to be converted to reflect its actual work potential. The overall specific exergy is defined as

$$E_{spec} = \frac{1}{N_{CO_2} MW_{CO_2}} \left(Q \left(1 - \frac{T_0}{T_{reg}} \right) + W \right) \tag{6}$$

where T_0 is the ambient temperature and T_{reg} is the temperature of regeneration. The thermal energy demand required for the TVSA cycle is determined by integrating the heat flow supplied to the column via external heating, $\dot{Q}_{in}$, during the desorption step

$$Q = \int_0^{t_{cycle}} \dot{Q}_{in} \, dt$$
$$= \int_0^{t_{cycle}} \left[\int_0^L h_W(T_{wf} - T_w) 2\pi R_{out} \, dz \right] dt \tag{7}$$

The electrical energy demand is equal to the sum of the blower and vacuum pump energy demand, the latter being described as an isothermal compression

$$W = \int_0^{t_{cycle}} [\dot{W}_{fan} + \dot{W}_{comp}] dt \tag{8}$$

where

$$\dot{W}_{fan} = \frac{1}{\eta_{fan}} \dot{V}(p_{in} - p_{out}) \tag{9}$$

$$\dot{W}_{comp} = \frac{1}{\eta_{comp}} \dot{n} RT \ln \left(\frac{p_H}{p_L} \right) \tag{10}$$

where $\dot{V}$ is the volumetric flow rate of gas fed to the column, $\eta_{fan} = 0.5$ is the efficiency of the blower, and $\dot{n}$ is the molar flow rate of gas processed through the vacuum pump, which compresses the gas from vacuum pressure p_L to atmospheric pressure p_H with an efficiency of $\eta_{comp} = 0.3$.[32,63]

2.6. Sensitivity Analysis. Among the various degrees of freedom in designing cyclic adsorption processes, three operating parameters have been identified as particularly influential on the DAC TVSA cycles. These are (1) the duration of the adsorption step, denoted as t_A; (2) the molar flow rate of air during adsorption, represented as $\dot{n}$; and (3) the duration of the desorption step, t_D. In DAC processes, where CO_2 recovery is not a stringent constraint, both the feed flow rate and the duration of the adsorption step can be adjusted freely. Longer adsorption times can increase cyclic capacities but might increase sorbent/volume demand, whereas higher flow rates can reduce this demand but potentially increase specific energy demands. By varying these parameters, we can identify the range of conditions that result in the trade-off that minimizes sorbent/volume demand on the one hand and blower requirements on the other hand. Flow rates that achieve superficial velocities of up to 2.4 m s^{-1}, at an average column pressure of 1 bar, have been assessed. Additionally, variations in the desorption step duration were examined to determine their effects on overall cyclic capacity and the demands for heat and vacuum power. A comprehensive parametric analysis of these decision variables
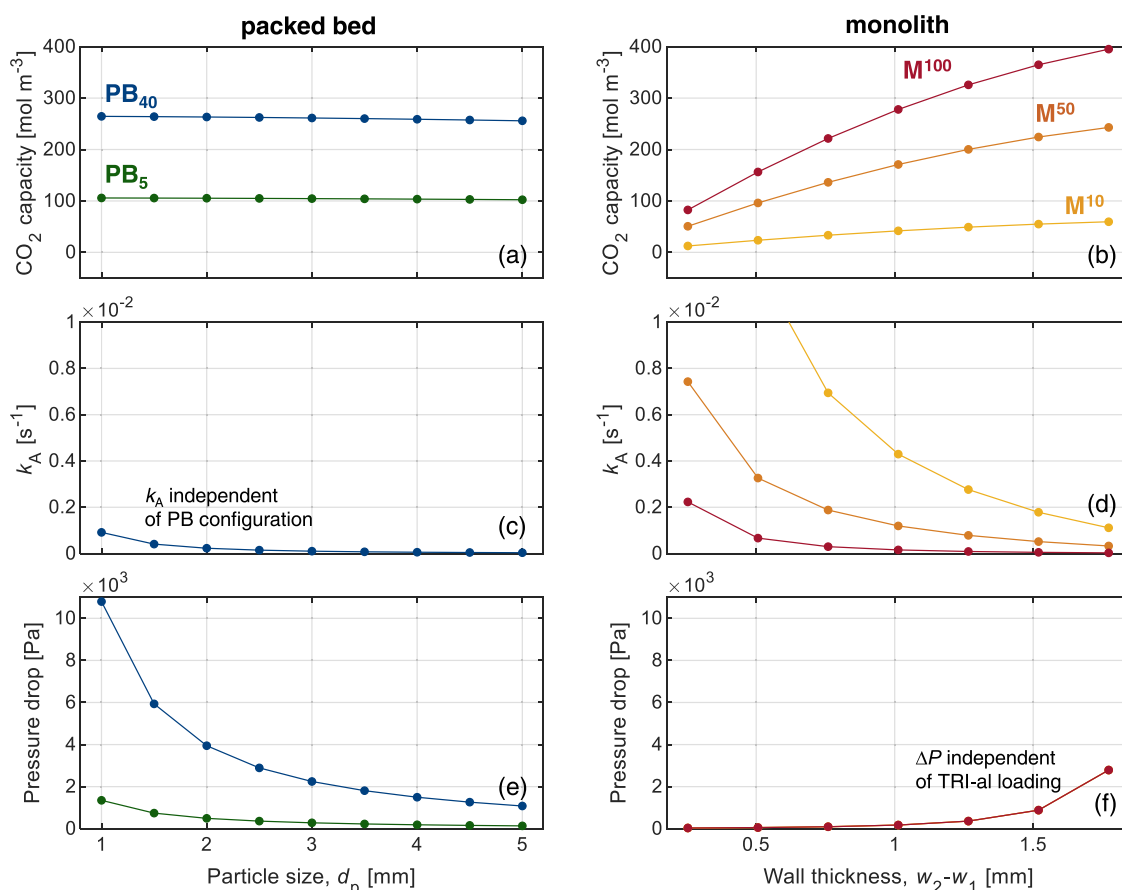
Figure 3. Fundamental properties of packed bed and monolith contactors evaluated against pellet particle size and monolith wall thickness, respectively: (a, b) CO_2 equilibrium capacity at feed conditions (y_{in} = 400 ppm, 25 °C, 1 bar); (c, d) mass transfer coefficient of the adsorption step; and (e, f) pressure drops for an average velocity of 0.8 ms^{-1}. The pressure drop across the entire column is given only for comparison. In the simulations, the momentum balance was estimated within specific control volumes using the system of PDEs outlined in Table S4.

was conducted to calculate sorbent and volume demand as well as specific exergy requirements. The computed results yielded feasible operating regions and associated Pareto fronts, which represent optimal trade-offs between minimizing sorbent and volume requirements on the one hand and minimizing specific exergy requirements on the other. From the range of conditions explored, the points along the Pareto front are such that no singular set of decision variables improves the two KPIs considered simultaneously. The ranges of the decision variables for all simulations are summarized in Table 2.

2.7. Impact of Assumptions. In this work, we make three assumptions that deserve being discussed: (1) H_2O is not included in the adsorption modeling; (2) TRI-al loadings in the monolith range from 10 to 100 wt %; and (3) the regeneration pressure is 10 mbar. These assumptions result from our decision to use experimentally characterized thermodynamic and kinetic adsorption data from TRI-al pellets and a TRI-al-coated monolith (Section 2.1). Given that the objective of this research is to compare TVSA cycle results between packed bed and monolith contactor geometries, it is crucial to clarify how our assumptions may influence the results.

The TRI-al pellets and TRI-al-coated monolith possess well-characterized experimental thermodynamic and kinetic data for single-component CO_2 adsorption. However, $CO_2–H_2O$ coadsorption on these materials has not been characterized yet. According to Young et al., inaccuracies in modeling binary isotherms can lead to divergent TVSA outcomes.[12] Rather than

introducing potential errors by inaccurately modeling water adsorption, we opted to rely on the validated dry data available for these materials and present results under dry conditions to establish a baseline for comparing the different contactors. Although this approach allows for an assessment of the contactors' geometric properties in terms of relative performance, we acknowledge that excluding water from our simulations may have a significant limitation on the quantitative outcomes.

Achieving up to 100% TRI-al monoliths is yet unverified in practice, but significant active sorbent loadings on monoliths have been achieved in the literature, with direct extrusion and postfunctionalization methods achieving up to 100 wt %.[28,35,64] Industry patents suggest that 80 wt % γ-alumina washcoats are achievable,[65] while the potential to produce 100 wt % γ-alumina monoliths has been demonstrated by Corning.[35] Further validation of triamine grafting on 100% γ-alumina monoliths is necessary but beyond the scope of this study. In our research, we explore monoliths with TRI-al loadings up to 100% in order to determine whether they are even desirable.

Lastly, in selecting the vacuum pressure for regeneration, we are confronted with two constraints. First, to ensure a positive cyclic capacity of CO_2 on TRI-al, we necessitate low regeneration pressures (see Figure S1). On the other hand, we need to be mindful of the industrial implications of working at low pressures. Low regeneration pressures raise vacuum pump energy demand, which we have incorporated into our results, raising the costs of operation (OPEX). Moreover, low
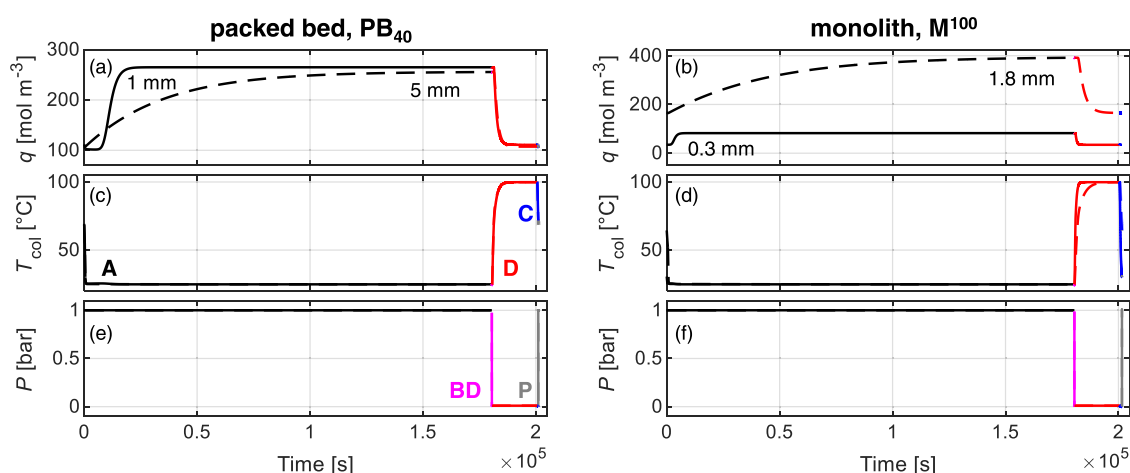
Figure 4. TVSA results showing cyclic steady-state profiles for t_A = 180,000 s, t_D = 20,000 s, and n = 2 mmol s^{-1} (ca. 0.4 m s^{-1}) for each cycle step. For PB$_{40}$, we compare 1 mm pellets (solid line) vs 5 mm pellets (dashed line), and for M^{100}, we compare 0.3 mm monolith walls (solid line) vs 1.8 mm walls (dashed line). Subfigures are divided into (a, b) CO$_2$ loading at the column exit, (c, d) column temperature, and (e, f) pressure profiles at the column exit.

regeneration pressures impact capital costs (CAPEX) because of the requirement for advanced industrial vacuum pumps, effective sealing techniques, and robust structural integrity of the contactor module's inlet. These considerations impact equally all of the designs analyzed in this work and, therefore, not the conclusions about their relative merits.

3. ANALYSIS OF CONTACTOR GEOMETRIC CHARACTERISTICS

Figure 3 shows the influence of sorbent size (pellet diameter and monolith wall thickness), TRI-al loading in monoliths, and packed bed configuration on key metrics in adsorption. These include CO$_2$ adsorption capacity per unit contactor volume, the adsorption mass transfer coefficient (k_A), and the pressure drop across the column during adsorption. This figure serves to quantitatively assess the advantages and drawbacks of the two structures.[28] The CO$_2$ capacity per contactor volume, $q_{V,\mathrm{in}}^*$, is computed as follows

$$q_{V,\mathrm{in}}^* = \omega \psi \rho_b q_{\mathrm{in}}^* \tag{11}$$

where q_{in}^* = 0.42 mol kg$_{\mathrm{TRI-al}}^{-1}$ is the CO$_2$ capacity per unit mass of TRI-al at equilibrium at the feed conditions, ρ_b is the bed density, ω is the TRI-al loading, and ψ is the bed-to-contactor volume ratio. The volumetric CO$_2$ capacity of PB$_5$ is significantly lower than that of PB$_{40}$ due to the effect of ψ. In both configurations, changes in pellet size barely alter the overall CO$_2$ capacity due to minimal variation in bed porosity with d_p (Figure S3(a)). Instead, variations in wall thickness significantly alter the overall bed porosity of the monolith (Figure S3(b)), consequently affecting the total TRI-al content in the contactor and resulting in a wide range of achievable CO$_2$ capacities, further amplified by the variation in the TRI-al loading. Overall, despite the variability introduced by these factors, the range of CO$_2$ capacities achieved in monolith configurations is comparable to that observed in packed beds.

The mass transfer coefficient during the adsorption step is computed from eq 2 using the correlations presented in Table S5 considering an average feed velocity of u_s = 0.8 m s^{-1} (Figure 3(c,d)). The resulting breakdown of k_A in terms of k_f, k_p, and k_s is shown in Figure S4(a,b) in the Supporting Information. In both the packed bed and monolith configurations, decreasing the sorbent size increases the mass transfer coefficients due to shortened diffusion paths, as expected. Despite having lower surface areas compared to pellet sorbents, we observe higher mass transfer coefficients in monoliths compared to pellets. This is primarily attributed to the significantly thinner wall thicknesses achievable in monoliths, providing a distinct advantage over pellets.[28,41,47] In the monoliths, both the variation in w_{wall} and in TRI-al loading result in a trade-off between the CO$_2$ capacity and kinetics. Indeed, kinetics are inversely proportional to the TRI-al loading, as influenced by the $q_{V,\mathrm{in}}^*/c_{\mathrm{in}}$ factor in the computation of k_A (see Figure S2).

The pressure drop across the contactor, as shown in Figure 3(e−f), is computed from eq (S10) for the packed bed and eq (S11) for the monolith, considering an average bed velocity of u_s = 0.8 m s^{-1}. We observe a substantial decrease in pressure drop levels in the PB$_5$ configuration compared to those in the PB$_{40}$ configuration, as expected. At this velocity, operation with the PB$_5$ configuration yields pressure drop levels similar to those of the monoliths. However, the packed beds and the monoliths exhibit contrasting trends: smaller pellets offer more resistance to flow in packed beds, thereby increasing the pressure drop, whereas thinner walls in monoliths lead to lower pressure drops due to the larger channel width. Consequently, the observed trade-off between pressure drop and kinetics given upon variation in pellet size does not apply to monoliths, where thinner walls simultaneously yield faster kinetics and a lower pressure drop. However, the CO$_2$ capacity is lower in monoliths with thin walls. Indeed, determining the optimal contactor configuration is nontrivial, as no single configuration simultaneously offers the highest CO$_2$ loadings, fastest mass transfer, and lowest pressure drop over the others. Several trade-offs have been identified: (1) PB$_{40}$ vs PB$_5$: CO$_2$ loading vs pressure drops, (2) d_p: kinetics vs pressure drops, (3) M^{10} vs M^{100}: kinetics vs CO$_2$ loadings, and (4) w_{wall}: kinetics and pressure drop vs CO$_2$ loadings. While detailed TVSA modeling is essential for determining the optimal contactor configuration and operational parameters of the DAC cycle, the observed trade-offs provide a foundational basis for contactor design and enhance our understanding of the TVSA modeling outcomes. Note that we have chosen to fix the monoliths' CPSI to 100 for this study, though it can be varied as a parameter. To illustrate the influence of CPSI on capacity, mass transfer, and pressure drop, Figure S5

Table 3. TVSA Results in Terms of CO$_2$ Cyclic Capacity, Heat, and Electrical Energy Demand for the Simulations Presented in Figure 4

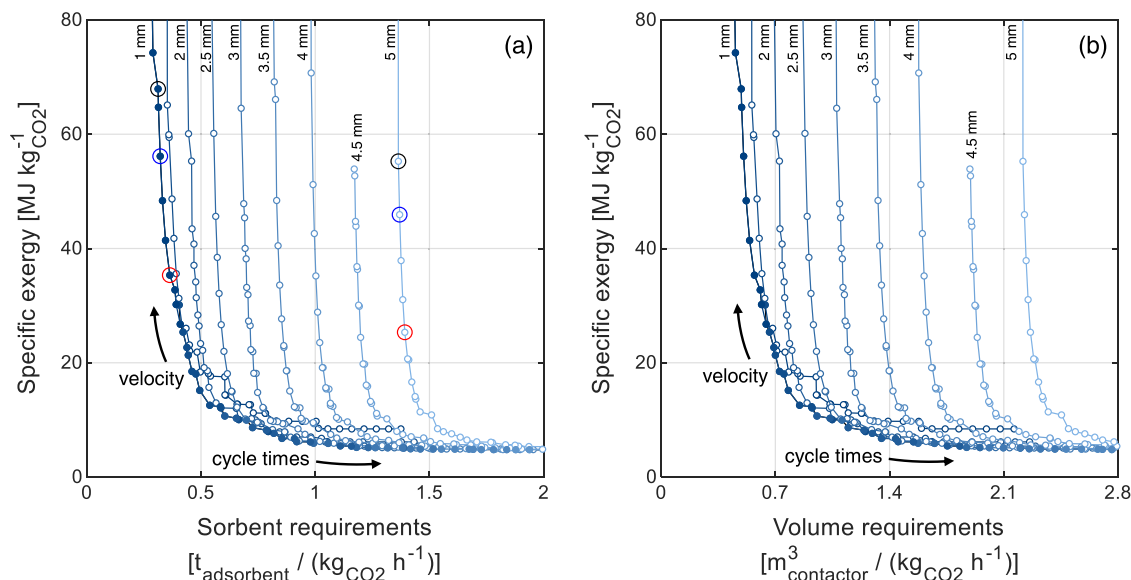|		PB$_{40}$		M^{100}	
	units	d_p = 1 mm	d_p = 5 mm	w_{wall} = 0.3 mm	w_{wall} = 1.8 mm
Δq_{CO_2}	[mmol]	78	75	24	115
Q	[MJ]	0.04	0.04	0.023	0.052
Q_{spec}	[MJ kg^{-1}]	11.8	12	22	11.4
W	[MJ]	0.7	0.06	0.006	0.33
W_{spec}	[MJ kg^{-1}]	195.4	17.1	5.9	65.9

Figure 5. Pareto sets obtained by varying t_A, t_D, and u_s on the TVSA cycle for PB$_{40}$ with pellet sizes in the range of 1−5 mm (dark blue to light blue lines), generated from simultaneously minimizing specific exergy and minimizing (a) sorbent requirements; or (b) volume requirements (design variables in Figure S6). The hollow markers in red, blue, and black highlight points of the 1 mm and 5 mm Pareto curves, which correspond to feed velocities of 0.72, 0.95, and 1.04 m/s, respectively. All points respect a minimum CO$_2$ purity requirement in the product stream of 99%.

compares the effects of using 200 and 400 CPSI against 100 CPSI for the M^{100} monolith. The impact of varying CPSI on cycle operation lies beyond the scope of this work but may be explored in future studies.

4. TVSA RESULTS FOR PB$_{40}$ AND M^{100}

In this section, we present a comparative assessment of contactors PB$_{40}$ and M^{100}, which have the same amount of active phase and the same volume (5 cm diameter and 40 cm length). The differences between these two contactors are accounted for using the corresponding mathematical description of bed porosity (Tables S2 and S3), mass transfer correlations (Table S5), and momentum balance (Table S4). We analyzed these differences by analyzing the cyclic steady-state profiles obtained in simulations at identical operating conditions, the results of the sensitivity analysis, and the effect of pellet size and monolith wall thickness on the DAC performance.

4.1. Cyclic Steady-State Profiles. The adsorbed-phase concentration fronts (at the column exit), the column temperature profiles, and the downstream pressure for both PB$_{40}$ and M^{100} are shown in Figure 4 for the smallest and largest particle size for PB$_{40}$ or wall thickness for M^{100}. The operating conditions are chosen to illustrate differences in column profiles between the two contactors, though they are not yet optimized in terms of our KPIs; the adsorption step time of 180,000 s

ensures full saturation in all cases, while the desorption step time is set so as to exploit the maximum CO$_2$ cyclic capacity.

The PB$_{40}$ simulations using 1 and 5 mm pellets (Figure 4a) attain similar saturation capacities, yet the smaller pellets exhibit much faster adsorption kinetics due to faster pore diffusion. During regeneration, the adsorbed-phase concentration profiles of the two pellet sizes are very similar, as desorption is governed by the rate of heat transfer to the column, which is the same in the two cases (Figure 4c). This similarity stems from comparable total sorbent mass and CO$_2$ cyclic capacities in the two cases, resulting in similar thermal energy requirements for desorption (Table 3). However, the smaller pellets incur higher electrical energy requirements due to increased pressure drops.

The M^{100} monolith with thinner walls facilitates rapid mass transfer yet substantially lower cyclic capacities relative to that with thicker walls. Additionally, the monolith with 0.3 mm walls exhibits reduced electrical and thermal energy demands due to decreased pressure drops and less thermal mass during regeneration. Nonetheless, the low cyclic capacity of this thin-walled monolith results in higher specific thermal energy requirements than the thick-walled monolith.

4.2. Pareto Fronts. The results of the sensitivity analysis on t_A, t_D, and u_s for the PB$_{40}$ contactor are shown in Figure 5a in the exergy-sorbent requirement plane and in Figure 5b in the exergy-volume-requirement plane. A Pareto optimum curve was generated for each pellet size, represented by a color ranging

from dark to light blue as d_p increases. All points on these curves meet a minimum CO_2 purity constraint of 99%. The points displayed in subfigures (a) and (b) are related by the expression $\hat{S} = \rho_b(d_p)\psi\hat{V}$ for each pellet size, with the corresponding design variables shown in Figure S6.

The convolution of the individual Pareto curves for each pellet size forms the overall Pareto curve for PB$_{40}$, shown by the solid markers in Figure 5. Smaller pellets facilitate rapid cycling due to faster mass transfer kinetics, which reduces sorbent and volume use while leading to higher specific exergy requirements. Larger pellets reduce specific exergy costs but increase the sorbent demands necessary for achieving the targeted CO_2 output. Notably, there exists a critical minimum sorbent and volume requirement for each pellet size, below which it is not possible to operate. This minimum increases with pellet size as a result of increasing mass transfer resistances with d_p, which limit adsorption rates and cap the maximum practical air velocity for operation. Surpassing this operational velocity increases specific exergy requirements to capture equivalent amounts of CO_2 without corresponding reductions in cycle times (Figure S6).

Figure 6 depicts the CO_2 loading profiles during adsorption for the three highlighted points on the 1 and 5 mm Pareto fronts,
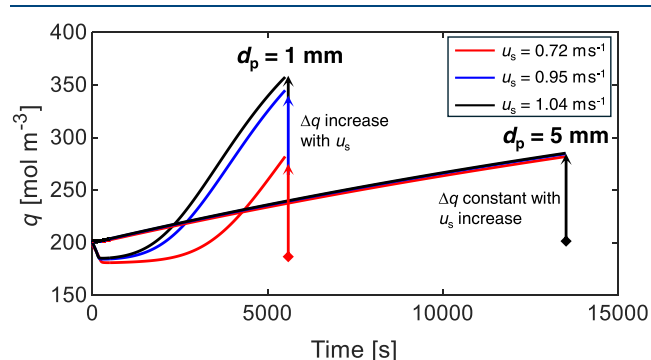

Figure 6. Effect of increasing feed velocity on the CO_2 loading profiles at $z = L$ for 5 mm pellets (light blue) and 1 mm pellets (dark blue) on Δq in the PB$_{40}$ contactor. The simulations derive from the TVSA model results taken from the Pareto curves in Figure 5 with $t_A = 13{,}450$ s, $t_D = 4000$ s for the points on the 5 mm Pareto curve and $t_A = 4450$ s, $t_D = 5000$ s for the points on the 1 mm Pareto curve.

whose simulations yielded equal cycle times at three different feed velocities. The adsorption rate of the 5 mm pellets is minimally affected by changes in velocity, as mass transfer kinetics govern the adsorption rate already at 0.72 m s^{-1}; thus, increasing velocity does not result in any additional benefits.[2,23,61] On the other hand, operating at the same three velocities with 1 mm pellets increases cyclic capacity as u_s increases due to reduced mass transfer kinetic limitations. Thus, for 1 mm pellets, higher velocities inevitably increase exergy demand but also decrease the contactor volume or the sorbent mass needed for a desired CO_2 production rate, in contrast to the 5 mm pellets.

The exergy-sorbent requirements and exergy-volume requirements of Pareto fronts for all wall thicknesses considered for M^{100} are shown in Figure 7 for a purity specification of 99%. Similar to PB$_{40}$, the two metrics on the horizontal axes are related by the expression $\hat{S} = \rho_b(w_{wall})\psi\hat{V}$ for each wall thickness, and the corresponding design variables are shown in Figure S7.

The overall Pareto curve in Figure 7a is limited to wall thicknesses between 0.3 and 0.8 mm. Thinner walls simulta-

neously improve the kinetics and pressure drop (Figure 3), thereby reducing cycle times and specific exergy needs. Thus, wall sizes above 0.8 mm are disadvantageous. The points on the Pareto curve in Figure 7b, derived from the same simulations as those in Figure 7a, do not show a consistent reduction in volume requirements with a decrease in w_{wall} within the specified operating conditions. This reflects the trade-off between mass transfer kinetics and volumetric CO_2 capacity with varying wall thickness, as observed with reference to Figure 3. Indeed, in contrast to packed beds where the bed density is constant with d_p, bed density varies significantly with w_{wall} (see Figure S3). Thinner walls no longer result in the Pareto curve because, while they may be beneficial for sorbent requirements, they yield bed densities that are too low, thus not minimizing volume requirements. As a result, the overall Pareto curve consists of wall thicknesses between 0.5 and 1 mm.

The differences in the overall Pareto curves in Figure 7a and b show that the choice of wall thickness depends on whether the priority is to minimize sorbent material usage or to reduce the spatial and material requirements of the vessel components. These design decisions are ultimately determined by balancing the cost of the sorbent with the cost of vessel components and land use.

5. COMPARISON OF CONTACTORS

The overall Pareto curves obtained on all contactors considered, including the two packed bed configurations and monoliths with TRI-al loadings ranging from 30 to 100%, are shown in Figure 8. The design variables yielding the Pareto curves in subfigures (a) and (b) are the same for the two packed bed configurations but differ for the monoliths due to the varying impact of design variables and monolith wall thickness on the two sorbent and volume requirement metrics, as discussed in Section 4.2. The resulting design variables are shown in Figures S8 and S9 in the Supporting Information.

For all configurations in Figure 8, long cycle times and low feed velocities reduce specific exergy demand, and short cycle times and high feed velocities decrease sorbent and volume requirements (Figures S8 and S9). The relative position of the monolith Pareto fronts in Figure 8a shows a consistent increase in performance with rising TRI-al loading in terms of both specific exergy and sorbent requirements. Although not shown in the figure, simulations with TRI-al loadings of 80 and 90% yielded Pareto curves that are indistinguishable from those of the M^{100} monolith, suggesting that any loading above 80% exhibits equally good performance. The comparison between the PB$_5$ configuration and the standard configuration PB$_{40}$ reveals that PB$_5$ achieves similar sorbent requirements with reduced exergy demands. The best relative performance overall is observed for the PB$_5$ and the monoliths with high TRI-al loading, with similar performance in the low-exergy region (4–7 MJ kg^{-1} and 0.25–1 t/(kg h^{-1})). Beyond this region, M^{100} offers significant advantages over PB$_5$. First, it halves the sorbent requirements achievable with PB$_5$, which are limited by mass transfer constraints that impede reductions in cycle times despite increased velocities. This improvement is possible because monolith structures utilize thinner wall thicknesses than the smallest available pellet sizes, enhancing mass transfer kinetics and allowing operations at higher velocities to reduce both cycle times and sorbent requirements. This indicates that higher velocities are not universally beneficial for direct air capture; instead, the optimal velocity range depends on the specific contactor configuration. Second, the reduction in sorbent
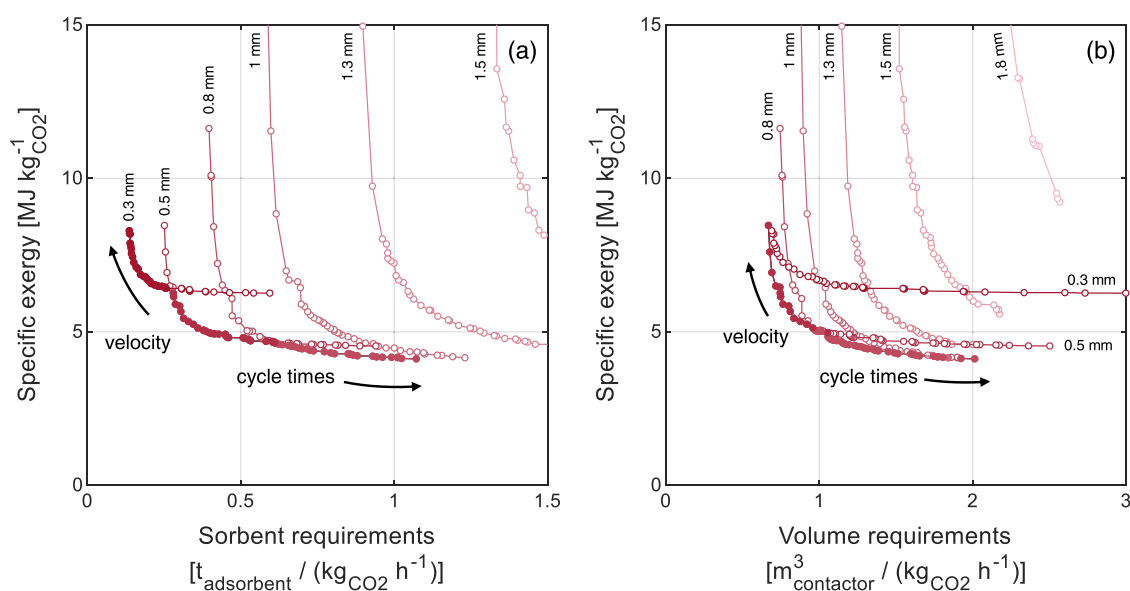
Figure 7. Pareto sets obtained by varying adsorption step time, desorption step time, and feed velocity on the TVSA cycle for M^{100} with wall thickness ranging from 0.3 to 1.8 mm (dark red to light red), expressed in terms of (a) sorbent-exergy demand and (b) contactor volume-exergy demand. The design variables for subfigures (a) and (b) are the same and are shown in Figure S7. All points respect a minimum CO_2 purity requirement in the product stream of 99%.
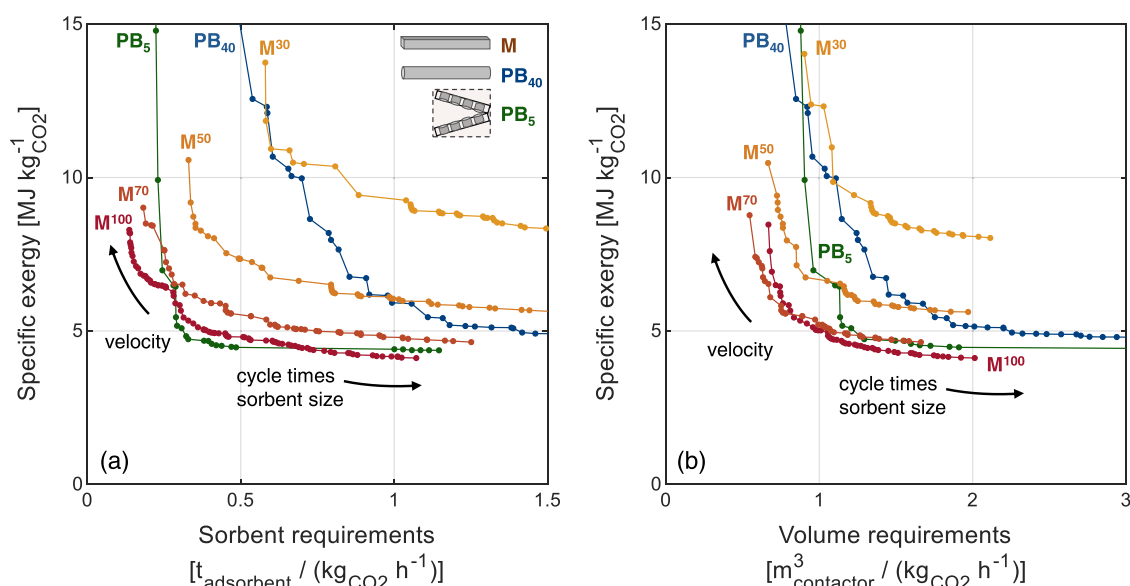

Figure 8. Pareto optimal curves obtained from the sensitivity analysis for the monoliths with a TRI-al content of 10, 30, 50, 70, and 100% (M^{10}, M^{30}, M^{50}, M^{70}, and M^{100}, respectively) and for the packed bed of 40 and 5 cm in length (PB_{40} and PB_5, respectively), considering all wall thicknesses and pellet sizes. The Pareto curves result from minimizing specific exergy and minimizing (a) sorbent requirements or (b) volume requirements.

demand in M^{100} is achieved with only a minor increase in exergy demand thanks to the dual benefits of thin walls, which not only enhance kinetics but also reduce pressure drop. This is not the case in packed beds where operating at higher velocities with smaller pellets than those considered might further decrease sorbent demands but at the cost of substantially increased exergy demand due to elevated pressure drop levels.

The analysis of specific exergy demand and volume requirements in Figure 8b demonstrates notable variations in the relative performance of the different contactors compared to those in Figure 8a. The substantial benefits associated with the PB_5 configuration relative to all other contactors become less pronounced when considered in terms of the total contactor volume. This reduction in effectiveness is due to the packed beds

occupying only $\psi = 40\%$ of the contactor volume, a necessary but undesirable consequence of the use of thin beds in such a configuration. The volume ratio that the packed beds occupy may change if the angle between the plates that hold them is lowered. However, such changes could alter the fluid dynamics within the contactor, potentially leading to variable air flow rates across different beds and challenging the assumption of uniform velocity. Furthermore, to reduce volume requirements, it becomes apparent that high TRI-al loadings do not consistently enhance performance. Instead, there appears to be an optimal loading below 100% that reduces volume requirements, illustrating the fundamental trade-off between mass transfer kinetics and volumetric CO_2 capacity as shown in Section 3. This result suggests that contrary to the findings for sorbent
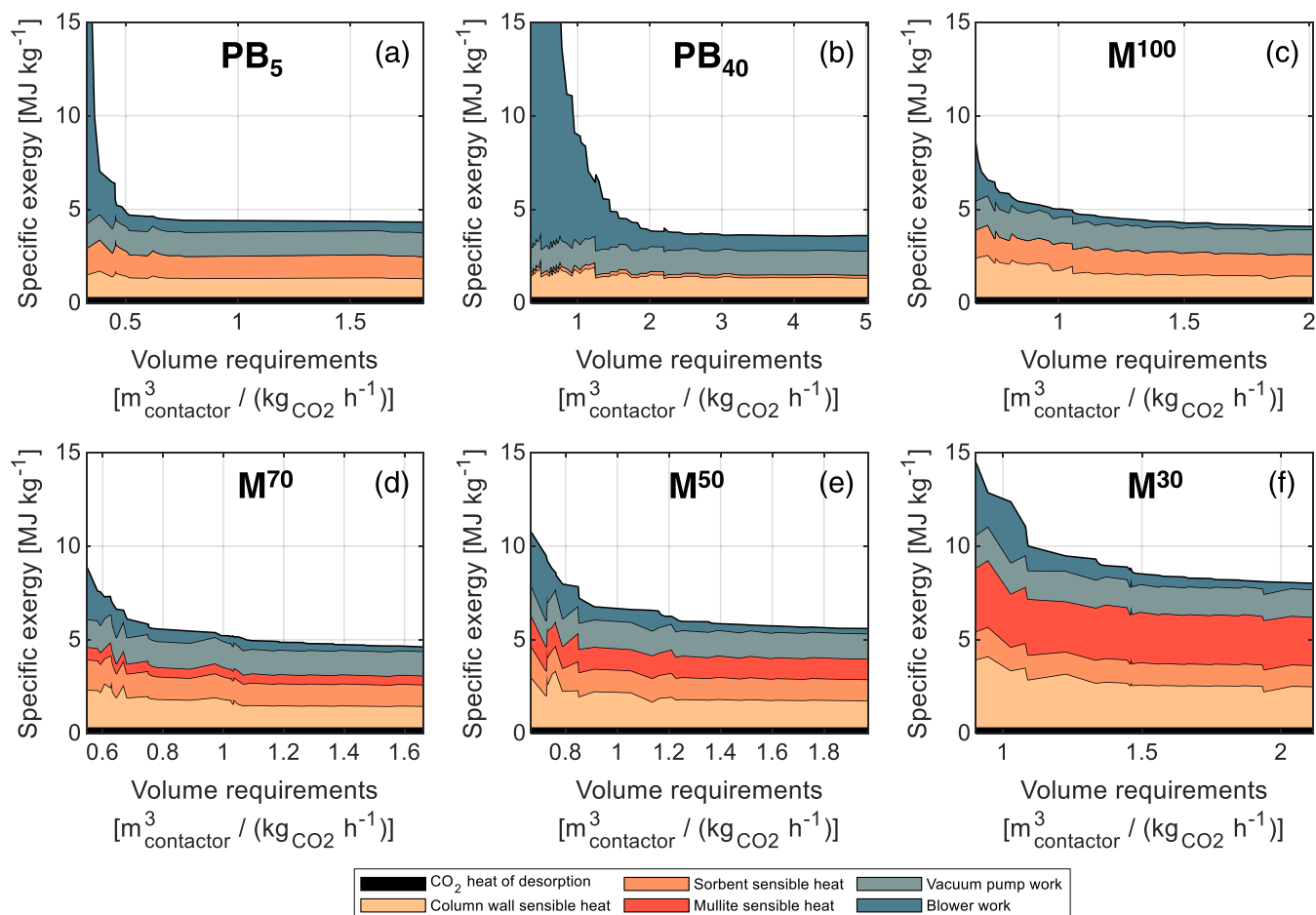
Figure 9. Breakdown of exergy demand for the Pareto fronts of Figure 8b, including the electrical energy (in blue) associated with the blowers and vacuum pumps and the sensible heat (in red) of the column wall, mullite, and sorbent and the CO_2 heat of desorption (in black).

Table 4. Comparison of PB$_5$ and M^{100} with other DAC TVSA Modeling Works[2,12,25,37,66]

	Q_{spec} [MJ kg^{-1}]	W_{spec} [MJ kg^{-1}]	E_{spec} [MJ kg^{-1}]	$P_V \times 10^{-3}$ [kg m^{-3} h^{-1}]	refs
Packed Bed Contactors					
Packed bed PB$_5$	12.6−15.3	1.8−11.7	4.4−14.8	0.2−1.1	
Young et al., mechanistic	8.8−9.3	0.8−1.2	2.5−2.7	2.6−3.3	12
Sabatino et al., E-A	n/a	n/a	2−12	0−1	25
Climeworks	11.9	2.52	4.9	0−1	25,66
Monolith Contactors					
Monolith M^{100}	13−26	1.5−3.1	4.1−8.3	0.2−1.5	
Sinha et al., MIL-101(Cr)-PEI-800	9.7	0.8	n/a	n/a	2
Sinha et al., mmen-Mg$_2$(dobpdc)	4.5	0.7	n/a	n/a	2
Sinha and Realff, MOF (generic)	1.9−19.3	0.1−3.8	n/a	n/a	37

requirements, the largest TRI-al loadings might not always be ideal. With the relative differences observed in Figures 8a and b, it is clear that the choice of contactor design will hinge on balancing the costs of adsorbent materials and vessel components within the overall capital expenditure.

The specific exergy breakdown for the points along the Pareto curves in Figure 8b is shown in Figure 9. The exergy breakdown includes the electrical energy demands for blower and vacuum pump operation, the thermal energy required for CO_2 desorption, and the parasitic thermal load, which encompasses all additional heat demand during regeneration exceeding that specifically needed for CO_2 desorption. This includes energy utilized to raise the temperature of the contactor walls, the mullite support (where applicable), and the adsorbent to the

desired desorption temperature. For all contactors, the decrease in volume requirements is mostly caused by an increase in blower usage, which is particularly prominent in the packed bed configurations. Additionally, the thermal energy demand largely exceeds the minimum thermal energy requirements for CO_2 desorption (in black). Specifically, the contactor wall's sensible heat contributes significantly to the heat demands; for packed beds, it accounts for 50% of the required heat, and for monoliths, it ranges from 50−70%. The large portion of column wall heat demand highlights an opportunity for design optimization by minimizing the wall-to-sorbent mass ratio, thereby reducing the thermal parasitic load.[37] As TRI-al loading diminishes and the relative mass of mullite increases, the thermal significance of mullite becomes apparent, thus highlighting a drawback caused

by the inert support materials in structured contactors.[36] Overall, monoliths primarily require thermal energy (60−80%), while packed beds require mainly electrical energy (40−99%), largely due to blower energy demand; this suggests that different approaches may be needed in the various contactors when coping with the corresponding energy demand.

To provide a broader context within the DAC literature and possibly to understand the quantitative implications of our assumptions (Section 2.7), we compare the energy requirements and volumetric productivity (defined as the inverse of the volume requirements, $P_V = \hat{V}^{-1}$) of PB_5 and M^{100} with the results of similar TVSA modeling works. We additionally include estimated data for Climeworks' DAC plant in Hinwil, offering insights into real-world packed bed configurations.[66] The ranges of specific heat, electricity, exergy, and cyclic productivity (when available) are reported in Table 4. For PB_5, we consider the simulation yielding E_{spec} = 15 MJ kg^{-1} as the upper limit due to the operational insignificance of the Pareto segment above this point. It is important to acknowledge that variations in sorbent and contactor selection, cycle design, and model assumptions distinguish each study. We outline the primary differences in our comparison.

Both Young et al. and Sabatino et al. explored TVSA cycles with packed bed geometries.[12,25] Young et al. considered a thin packed bed (L = 1 cm) with Lewatit VP OC 1065 as sorbent, deriving k_{CO2} = 0.008 s^{-1} from breakthrough experiments. Sabatino et al. evaluated the performance of multiple sorbents sourced from DAC literature in a TVSA cycle using a multibed packed bed configuration (5 cm length, 5 mm diameter) with ψ = 0.4. We take their values for the E-A sorbent with k = 0.0001 s^{-1} for comparison. A critical difference in our study is the absence of water, which in their models increased not only the CO_2 capacities but also the heat demand for H_2O desorption, accounting for 40−50% of total heat requirements in their simulations. While we omitted water, we incorporated the thermal mass of the column wall, a factor that accounts for approximately 50% of our estimated heat requirements and that was overlooked in these studies even though the heat was provided externally. Estimating the thermal impact of water desorption requires detailed data on the cyclic capacities of H_2O and CO_2 under humid conditions; however, adjusting for these factors suggests that substituting the wall thermal load with water effects might yield comparable Q_{spec} values to our current estimates. Our exergy range and productivity values align closely with those reported by Sabatino et al. and the estimates for Climeworks' Hinwil plant but are lower Young et al.'s estimates due to their assumed ψ = 1 for productivity calculations.

The results of M^{100} are compared to two studies focusing on metal−organic framework (MOF) sorbents coated on honeycomb monoliths. Sinha et al. compared two MOFs on the same monolith contactor geometry, employing a steam-assisted TVSA cyclic process during regeneration but neglecting humidity effects on adsorption.[2] Our results reveal notably higher W_{spec} and Q_{spec} compared to their findings, mainly due to low regeneration pressures and sensible heat in the contactor wall. Indeed, a positive aspect of steam condensation, as considered in their work, is its potential to reduce or eliminate the need for indirect heating and mitigate heat losses in the contactor walls. Furthermore, it may act as a displacing agent during desorption (thus enabling higher regeneration pressures[32]), improve heat distribution for contactors with large cross sections, and allow for shorter desorption times. However, steam modeling necessitates accurate $CO_2−H_2O$ binary

isotherms, particularly at elevated temperatures.[12,67] Our findings align more closely with the work by Sinha and Realff,[37] who emphasized the thermal impacts of the contactor wall in their sensitivity analysis, showing that higher contactor to adsorbent mass ratios lead to increased Q_{spec} and W_{spec}. While there is better agreement concerning energy requirements with the second work, the absence of productivity data precludes a thorough comparison.

6. CONCLUSIONS

This study assessed the performance of packed bed and monolith contactors for DAC processes, focusing on geometric aspects of the contactors, such as sorbent size, TRI-al content, and packed bed configurations. A five-step TVSA cycle was designed, and a sensitivity analysis of its operating parameters was conducted. Despite the limitations of this study (Section 2.7), the analysis of specific exergy demand, sorbent, and volume requirements provided significant insights into each configuration's advantages and operational feasibility.

In terms of packed bed configurations, PB_5 outperformed PB_{40} entirely and was competitive with monoliths with TRI-al loadings above 80% when minimizing exergy against sorbent requirements. However, the extra volumes required for its multibed configuration resulted in larger volume needs, making it less competitive compared to the other contactors examined.

Minimizing the sorbent requirements and the volume requirements yielded different results in terms of monolith design: thinner walls reduced sorbent needs but resulted in lower bed densities, which were not advantageous for minimizing volume. Overall, monolith performance improved with increased TRI-al content, with marginal gains beyond 70 wt %. This suggests that a maximum TRI-al loading is not necessarily required.

Overall, the most significant improvement in monolith performance over PB_5 was not merely energy efficiency but the achievement of faster cycles and, thus, lower overall sorbent and volume requirements. This positive result stems from the inherent advantages of monolith structures, which include the ability to produce thin walls, effectively reducing the characteristic length associated with mass transfer limitations and pressure drop. Additionally, operating at maximum velocities is not an optimal strategy; instead, the optimal operational feed velocity is fundamentally limited by the design of the contactor itself.

The decision regarding the choice, design, and operation of the contactors ultimately depends on balancing relative cost-limiting factors within overall costs. When the cost of adsorbent material is significant, optimizing for sorbent usage becomes crucial to minimize material consumption. When the cost of vessel components dominates, the focus shifts to optimizing for volume, aiming to reduce the spatial and material requirements of the vessel components.

■ ASSOCIATED CONTENT

Ⓢ Supporting Information

The Supporting Information is available free of charge at https://pubs.acs.org/doi/10.1021/acs.iecr.4c02303.

> Additional information on the adsorption model equations, axial dispersion, and mass transfer correlations and design variables that form the Pareto optimal curves is available in the S.I. (PDF)

■ AUTHOR INFORMATION

Corresponding Author

Marco Mazzotti − *Institute of Energy and Process Engineering, ETH Zurich, 8092 Zurich, Switzerland;* ● orcid.org/0000-0002-4948-6705; Phone: +41 44 632 24 56; Email: marco.mazzotti@ipe.mavt.ethz.ch; Fax: +41 44 632 11 41

Author

Valentina Stampi-Bombelli − *Institute of Energy and Process Engineering, ETH Zurich, 8092 Zurich, Switzerland*

Complete contact information is available at:
https://pubs.acs.org/10.1021/acs.iecr.4c02303

Notes

The authors declare no competing financial interest.

■ ACKNOWLEDGMENTS

■ NOTATION

Roman Symbols

A	column cross-section $[\mathrm{m}^2]$
b_0	Toth affinity coefficient at reference temperature $[\mathrm{kPa}^{-1}]$
c	gas-phase concentration $[\mathrm{mol\ m}^{-3}]$
d_p	pellet diameter $[\mathrm{m}]$
d_pore	diameter of the γ-alumina pore $[\mathrm{m}]$
D	column diameter $[\mathrm{m}]$
D_al	effective diffusivity in the γ-alumina pockets $[\mathrm{m}^2\ \mathrm{s}^{-1}]$
D_p	effective diffusivity in the pellet pore $[\mathrm{m}^2\ \mathrm{s}^{-1}]$
D_m	molecular diffusion $[\mathrm{m}^2\ \mathrm{s}^{-1}]$
D_mullite	effective diffusivity in the mullite pores $[\mathrm{m}^2\ \mathrm{s}^{-1}]$
D_s	crystalline diffusivity $[\mathrm{m}^2\ \mathrm{s}^{-1}]$
D_L	axial dispersion coefficient $[\mathrm{m}^2\ \mathrm{s}^{-1}]$
h_L	heat transfer coefficient column wall $[\mathrm{J\ m}^{2-}\ \mathrm{s}^{-1}\ \mathrm{K}^{-1}]$
h_W	heat transfer coefficient wall heat jacket $[\mathrm{J\ m}^{2-}\ \mathrm{s}^{-1}\ \mathrm{K}^{-1}]$
k	LDF overall mass transfer coefficient $[\mathrm{s}^{-1}]$
k_f	film mass transfer coefficient $[\mathrm{s}^{-1}]$
k_f'	film mass transfer coefficient $[\mathrm{m\ s}^{-1}]$
k_p	pore mass transfer coefficient $[\mathrm{s}^{-1}]$
$k_\mathrm{p,al}$	mass transfer coefficient in the γ-alumina pocket mesopores $[\mathrm{s}^{-1}]$
$k_\mathrm{p,mullite}$	mass transfer coefficient in the mullite macropores $[\mathrm{s}^{-1}]$
k_s	solid mass transfer coefficient $[\mathrm{s}^{-1}]$
L	column length $[\mathrm{m}]$
M	molecular weight $[\mathrm{g\ mol}^{-1}]$
m_s	sorbent mass $[\mathrm{kg}]$
$\mathrm{MW}_{\mathrm{CO}_2}$	molecular weight of CO_2 $[\mathrm{g\ mol}^{-1}]$
$\dot{n}$	molar flow rate $[\mathrm{mol\ s}^{-1}]$
N	total number of cells in the monolith $[-]$
n_s0	Toth maximum capacity at reference temperature $[\mathrm{mol\ kg}^{-1}]$
p	pressure $[\mathrm{Pa}]$
p_H	atmospheric pressure $[\mathrm{Pa}]$
p_L	vacuum pressure $[\mathrm{Pa}]$
q	mass-based adsorbed-phase concentration $[\mathrm{mol\ kg}^{-1}]$
q_p	volume-based adsorbed-phase concentration $[= q\rho_\mathrm{p}]$ $[\mathrm{mol\ m}^{-3}]$
q^*	solid loading at equilibrium with c $[\mathrm{mol\ kg}^{-1}]$

r_1	internal hydraulic diameter of the square monolith channel[68] $[= 2w_1/\pi]$ $[\mathrm{m}]$
r_2	external hydraulic diameter of the square monolith channel[68] $[= (4w_{wall}w_2/\pi + r_1^2)^{0.5}]$ $[\mathrm{m}]$
r_al	radius of γ-alumina pockets $[\mathrm{m}]$
r_c	crystalline radius $[\mathrm{m}]$
r_p	pellet radius $[\mathrm{m}]$
Re	Reynolds number $[=\rho u_s d_\mathrm{p}/\mu]$ $[-]$
$\hat{S}$	sorbent requirements $[t_\mathrm{adsorbent}/(\mathrm{kg}_{\mathrm{CO}_2}\mathrm{h}^{-1})]$
Sc	Schmidt number $[=\mu/(\rho D_\mathrm{m})]$ $[-]$
Sh	Sherwood number $[-]$
t	time $[\mathrm{s}]$
T	temperature $[\mathrm{K}]$
t_0	Toth exponent at reference temperature $[-]$
T_0	reference temperature $[\mathrm{K}]$
T_H	high temperature of external jacket $[\mathrm{K}]$
T_L	low temperature of external jacket $[\mathrm{K}]$
u	interstitial velocity $[= u_s/\varepsilon]$ $[\mathrm{ms}^{-1}]$
u_s	superficial velocity $[\mathrm{ms}^{-1}]$
$\dot{V}$	volumetric flow rate of the gas feed $[\mathrm{m}^3\ \mathrm{s}^{-1}]$
$\hat{V}$	volume requirements $[\mathrm{m_{contactor}}^3/(\mathrm{kg}_{\mathrm{CO}_2}\mathrm{h}^{-1})]$
W	monolith width $[\mathrm{m}]$
w_1	monolith void channel width $[\mathrm{m}]$
w_2	monolith cell width $[w_2 = w_1 + w_{wall}]$ $[\mathrm{m}]$
W_fan	specific blower energy consumption $[\mathrm{MJ\ mol}^{-1}]$
w_wall	monolith wall thickness $[\mathrm{m}]$
x	dimensionless axial coordinate $[= z/L]$ $[-]$
y	CO_2 molar fraction $[-]$
z	axial coordinate $[\mathrm{m}]$

Greek Symbols

α	parameter of the Toth equation $[-]$
χ	parameter of the Toth equation $[-]$
ΔH_0	isosteric heat of adsorption $[\mathrm{kJ\ mol}^{-1}]$
Δp	pressure drop across the column $[\mathrm{Pa}]$
Δq	cyclic capacity of CO_2 $[\mathrm{mol\ kg}^{-1}]$
Δq_max	maximum cyclic capacity of CO_2 $[\mathrm{mol\ kg}^{-1}]$
ε	bed void fraction $[-]$
ε_a	TRI porosity $[-]$
ε_p	pellet/wall void fraction $[-]$
ε^*	total void fraction $[=\varepsilon + \varepsilon_\mathrm{p}\ (1-\varepsilon)]$ $[-]$
μ	dynamic viscosity $[\mathrm{Pa\ s}]$
ρ	air density $[\mathrm{kg\ m}^{-3}]$
ρ_b	bed density $[\mathrm{kg\ m_{BED}}^{-3}]$
ρ_p	sorbent density $[\mathrm{kg\ m_{SORBENT}}^{-3}]$
ρ_s	solid density $[\mathrm{kg\ m_{SOLID}}^{-3}]$
τ_al	γ-alumina tortuosity $[-]$
τ_mullite	mullite tortuosity $[-]$
ψ	bed-to-contactor volume ratio $[-]$
ω	TRI-al loading: active sorbent-to-total monolith mass ratio $[-]$

Subscripts and Superscripts

in   feed conditions

Acronyms

CDR	carbon dioxide removal
CPSI	cells per square inch
CSS	cyclic steady state
DAC	direct air capture
KPI	key performance indicator
LDF	linear driving force
MFC	mass flow controler
NET	negative emission technologies

■ REFERENCES

(1) IPCC; Kim, E.; Lee, W. et al. *IPCC Report Global Warming of 1.5 °C. An IPCC Special Report on the Impacts of Global Warming of 1.5 °C Above Pre-industrial Levels and Related Global Greenhouse Gas Emission Pathways, in the Context of Strengthening the Global Response to the Threat of Climate Change*, 2018; pp 17−20.

(2) Sinha, A.; Darunte, L. A.; Jones, C. W.; Realff, M. J.; Kawajiri, Y. Systems Design and Economic Analysis of Direct Air Capture of CO2 through Temperature Vacuum Swing Adsorption Using MIL-101(Cr)-PEI-800 and mmen-Mg2(dobpdc) MOF Adsorbents. *Ind. Eng. Chem. Res.* **2017**, *56*, 750−764.

(3) Keith, D. W.; Holmes, G., St.; Angelo, D.; Heidel, K. A Process for Capturing CO2 from the Atmosphere. *Joule* **2018**, *2*, 1573−1594.

(4) Ünveren, E. E.; Monkul, B. A.; Saroğlan, Å.; Karademir, N.; Alper, E. Solid amine sorbents for CO2 capture by chemical adsorption: A review. *Petroleum* **2017**, *3*, 37−50.

(5) Kong, F.; Rim, G.; Song, M. G.; Rosu, C.; Priyadarshini, P.; Lively, R. P.; Realff, M. J.; Jones, C. W. Research needs targeting direct air capture of carbon dioxide: Material & process performance characteristics under realistic environmental conditions. *Korean J. Chem. Eng.* **2022**, *39*, 1−19.

(6) Pang, S. H.; Lively, R. P.; Jones, C. W. Oxidatively-Stable Linear Poly(propylenimine)-Containing Adsorbents for CO2 Capture from Ultradilute Streams. *ChemSusChem* **2018**, *11*, 2628−2637.

(7) Gebald, C.; Wurzbacher, J. A.; Tingaut, P.; Zimmermann, T.; Steinfeld, A. Amine-based nanofibrillated cellulose as adsorbent for CO2 capture from air. *Environ. Sci. Technol.* **2011**, *45*, 9101−9108.

(8) Potter, M. E.; Lee, J. J.; Darunte, L. A.; Jones, C. W. Exploring steam stability of mesoporous alumina species for improved carbon dioxide sorbent design. *J. Mater. Sci.* **2019**, *54*, 7563−7575.

(9) Belmabkhout, Y.; Serna-Guerrero, R.; Sayari, A. Adsorption of CO2 -Containing Gas Mixtures over Amine-Bearing Pore-Expanded MCM-41 Silica: Application for Gas Purification. *Ind. Eng. Chem. Res.* **2010**, *49*, 359−365.

(10) Kwon, H. T.; Sakwa-Novak, M. A.; Pang, S. H.; Sujan, A. R.; Ping, E. W.; Jones, C. W. Aminopolymer-Impregnated Hierarchical Silica Structures: Unexpected Equivalent CO2 Uptake under Simulated Air Capture and Flue Gas Capture Conditions. *Chem. Mater.* **2019**, *31*, 5229−5237.

(11) Drechsler, C.; Agar, D. W. Investigation of water co-adsorption on the energy balance of solid sorbent based direct air capture processes. *Energy* **2020**, *192*, No. 116587.

(12) Young, J.; García-Díez, E.; Garcia, S.; Ireland, C.; Smit, B.; van der Spek, M. Investigating H2O and CO2 co-adsorption on amine-functionalised solid sorbents for direct air capture. *SSRN Electron. J.* **2021**, 1−7.

(13) Wiegner, J. F.; Grimm, A.; Weimann, L.; Gazzani, M. Optimal Design and Operation of Solid Sorbent Direct Air Capture Processes at Varying Ambient Conditions. *Ind. Eng. Chem. Res.* **2022**, *61*, 12649−12667.

(14) Wurzbacher, J. A.; Gebald, C.; Piatkowski, N.; Steinfeld, A. Concurrent Separation of CO2 and H2O from Air by a Temperature-Vacuum Swing Adsorption/Desorption Cycle. *Environ. Sci. Technol.* **2012**, *46*, 9191−9198.

(15) Wang, Y.; Rim, G.; Song, M. G.; Holmes, H. E.; Jones, C. W.; Lively, R. P. Cold Temperature Direct Air CO2 Capture with Amine-Loaded Metal-Organic Framework Monoliths. *ACS Appl. Mater. Interfaces* **2024**, *16*, 1404−1415.

(16) Custelcean, R. Direct air capture of CO2: Via crystal engineering. *Chem. Sci.* **2021**, *12*, 12518−12528.

(17) Heydari-Gorji, A.; Sayari, A. CO2 capture on polyethylenimine-impregnated hydrophobic mesoporous silica: Experimental and kinetic modeling. *Chem. Eng. J.* **2011**, *173*, 72−79.

(18) Serna-Guerrero, R.; Belmabkhout, Y.; Sayari, A. Further investigations of CO2 capture using triamine-grafted pore-expanded mesoporous silica. *Chem. Eng. J.* **2010**, *158*, 513−519.

(19) Serna-Guerrero, R.; Sayari, A. Modeling adsorption of CO2 on amine-functionalized mesoporous silica. 2: Kinetics and breakthrough curves. *Chem. Eng. J.* **2010**, *161*, 182−190.

(20) Gelles, T.; Rezaei, F. Diffusion kinetics of CO2 in amineimpregnated MIL101, alumina, and silica adsorbents. *AIChE J.* **2020**, *66*, 1−15.

(21) McQueen, N.; Gomes, K. V.; McCormick, C.; Blumanthal, K.; Pisciotta, M.; Wilcox, J. A review of direct air capture (DAC): scaling up commercial technologies and innovating for the future. *Prog. Energy* **2021**, *3*, No. 032001.

(22) Stampi-Bombelli, V.; Storione, A.; Grossmann, Q.; Mazzotti, M. On comparing packed beds and monoliths for CO2 capture from air through experiments, theory and modeling. *Ind. Eng. Chem. Res.* **2024**, *63*, 11637−11653.

(23) Tegeler, E.; Cui, Y.; Masoudi, M.; Bahmanpour, A. M.; Colbert, T.; Hensel, J.; Balakotaiah, V. A novel contactor for reducing the cost of direct air capture of CO2. *Chem. Eng. Sci.* **2023**, *281*, No. 119107.

(24) Young, J.; Mcilwaine, F.; Smit, B.; Garcia, S.; van der Spek, M. Process-informed adsorbent design guidelines for direct air capture. *Chem. Eng. J.* **2023**, *456*, No. 141035.

(25) Sabatino, F.; Grimm, A.; Gallucci, F.; van Sint Annaland, M.; Kramer, G. J.; Gazzani, M. A comparative energy and costs assessment and optimization for direct air capture technologies. *Joule* **2021**, *5*, 2047−2076.

(26) Balasubramaniam, B. M.; Thierry, P.-T.; Lethier, S.; Pugnet, V.; Llewellyn, P.; Rajendran, A. Process-performance of solid sorbents for Direct Air Capture (DAC) of CO2 in optimized temperature-vacuum swing adsorption (TVSA) cycles. *Chem. Eng. J.* **2024**, *485*, No. 149568.

(27) Yu, Q.; Brilman, D. W. Design Strategy for CO2 Adsorption from Ambient Air Using a Supported Amine Based Sorbent in a Fixed Bed Reactor. *Energy Procedia* **2017**, *114*, 6102−6114.

(28) DeWitt, S. J.; Sinha, A.; Kalyanaraman, J.; Zhang, F.; Realff, M. J.; Lively, R. P.; DeWitt, S. J.; Sinha, A.; Kalyanaraman, J.; Zhang, F.; Realff, M. J.; Lively, R. P. Critical Comparison of Structured Contactors for Adsorption-Based Gas Separations. *Annu. Rev. Chem. Biomol. Eng.* **2018**, *9*, 129−152.

(29) Yu, Q.; Brilman, W. A Radial Flow Contactor for Ambient Air CO2 Capture. *Applied Sciences* **2020**, *10*, 1080.

(30) Fasihi, M.; Efimova, O.; Breyer, C. Techno-economic assessment of CO2 direct air capture plants. *J. Clean. Prod.* **2019**, *224*, 957−980.

(31) Azarabadi, H.; Lackner, K. S. A sorbent-focused techno-economic analysis of direct air capture. *Appl. Energy* **2019**, *250*, 959−975.

(32) Stampi-Bombelli, V.; van der Spek, M.; Mazzotti, M. Analysis of direct capture of CO2 from ambient air via steam-assisted temperaturevacuum swing adsorption. *Adsorption* **2020**, *26*, 1183−1197.

(33) Gebald, C.; Piatkowskl, N.; Rüesch, T.; Wurzbacher, J. A. Low-Pressure Drop Structure of Particle Adsorbent Bed for Adsorption Gas Separation Process. International Parent Application, WO2014/170184AL2014.

(34) Min, Y. J.; Ganesan, A.; Realff, M. J.; Jones, C. W. Direct Air Capture of CO2 Using Poly(ethyleneimine)-Functionalized Expanded Poly(tetrafluoroethylene)/Silica Composite Structured Sorbents. *ACS Appl. Mater. Interfaces* **2022**, *14*, 40992−41002.

(35) Sakwa-Novak, M. A.; Yoo, C. J.; Tan, S.; Rashidi, F.; Jones, C. W. Poly(ethylenimine)-Functionalized Monolithic Alumina Honeycomb Adsorbents for CO2 Capture from Air. *ChemSusChem* **2016**, *9*, 1859−1868.

(36) Kulkarni, A. R.; Sholl, D. S. Analysis of equilibrium-based TSA processes for direct capture of CO2 from Air. *Ind. Eng. Chem. Res.* **2012**, *51*, 8631−8645.

(37) Sinha, A.; Realff, M. J. A parametric study of the techno-economics of direct CO2 air capture systems using solid adsorbents. *AIChE J.* **2019**, *65*, 1−8.

(38) Darunte, L. A.; Terada, Y.; Murdock, C. R.; Walton, K. S.; Sholl, D. S.; Jones, C. W. Monolith-Supported Amine-Functionalized Mg2(dobpdc) Adsorbents for CO2 Capture. *ACS Appl. Mater. Interfaces* **2017**, *9*, 17042−17050.

(39) Eisenberger, P.; Chichilnisky, G. Rotating Multi-Monolith Bed Movement System for Removing CO2 from the Atmosphere, US Patent, US10,512,880B2, 2019.

(40) Eisenberger, P. *Carbon Dioxide Capture/Regeneration Structures and Techniques*. 2012.

(41) Rezaei, F.; Webley, P. Optimum structured adsorbents for gas separation processes. *Chem. Eng. Sci.* **2009**, *64*, 5182−5191.

(42) Rezaei, F.; Webley, P. Structured Adsorbents in Gas Separation Processes. *Sep. Purif. Technol.* **2010**, *70*, 243−256.

(43) Mennitto, R. Modelling of Monoliths For Adsorption Processes. P.D. Thesis, The University of Edinburgh, 2021.

(44) Ahn, H.; Brandani, S. Dynamics of Carbon Dioxide Breakthrough in a Carbon Monolith Over a Wide Concentration Range. *Adsorption* **2005**, *11*, 473−477.

(45) Sharma, I.; Mennitto, R.; Friedrich, D.; Brandani, S. Combining the Nonuniform Structure and Flow Maldistribution for the Accurate Prediction of the Process Performance of Monolithic Adsorbent Systems. *Ind. Eng. Chem. Res.* **2020**, *59*, 3162−3172.

(46) Mennitto, R.; Sharma, I.; Brandani, S. Extruded monoliths for gas separation processes: Height equivalent to a theoretical plate and pressure drop correlations. *AIChE J.* **2022**, *68*, e17650 DOI: 10.1002/aic.17650.

(47) Rezaei, F.; Mosca, A.; Webley, P.; Hedlund, J.; Xiao, P. Comparison of traditional and structured adsorbents for CO2 separation by vacuum-swing adsorption. *Ind. Eng. Chem. Res.* **2010**, *49*, 4832−4841.

(48) Grossmann, Q.; Stampi-Bombelli, V.; Yakimov, A.; Docherty, S.; Copéret, C.; Mazzotti, M. Developing Versatile Contactors for Direct Air Capture of CO2 through Amine Grafting onto Alumina Pellets and Alumina Wash-Coated Monoliths. *Ind. Eng. Chem. Res.* **2023**, *62*, 13594−13611.

(49) Benyahia, F.; O'Neill, K. E. Enhanced voidage correlations for packed beds of various particle shapes and sizes. *Partic. Sci. Technol.* **2005**, *23*, 169−177.

(50) TAQA. *PORTHOS: Basis of Completion Design*, 2019.

(51) Equinor *Northern Lights Project Concept Report - RE-PM673−00001*, **2019**.

(52) Yu, Q.; Delgado, J. D. L. P.; Veneman, R.; Brilman, D. W. Stability of a Benzyl Amine Based CO2 Capture Adsorbent in View of Regeneration Strategies. *Ind. Eng. Chem. Res.* **2017**, *56*, 3259−3269.

(53) Casas, N.; Schell, J.; Pini, R.; Mazzotti, M. Fixed bed adsorption of CO2/H 2 mixtures on activated carbon: Experiments and modeling. *Adsorption* **2012**, *18*, 143−161.

(54) Schell, J.; Casas, N.; Marx, D.; Mazzotti, M. Precombustion CO2 capture by pressure swing adsorption (PSA): Comparison of laboratory PSA experiments and simulations. *Ind. Eng. Chem. Res.* **2013**, *52*, 8311−8322.

(55) Joss, L.; Gazzani, M.; Mazzotti, M. Rational design of temperature swing adsorption cycles for post-combustion CO2 capture. *Chem. Eng. Sci.* **2017**, *158*, 381−394.

(56) Garg, D. R.; Ruthven, D. M. Linear driving force approximations for diffusion controlled adsorption in molecular sieve columns. *AIChE J.* **1975**, *21*, 200−202.

(57) Shafeeyan, M. S.; Wan Daud, W. M. A.; Shamiri, A. A review of mathematical modeling of fixed-bed columns for carbon dioxide adsorption. *Chem. Eng. Res. Des.* **2014**, *92*, 961−988.

(58) Farooq, S.; Ruthven, D. M. Heat Effects in Adsorption Column Dynamics. 1. Comparison of One- and Two-Dimensional Models. *Ind. Eng. Chem. Res.* **1990**, *29*, 1076−1084.

(59) Haghpanah, R.; Majumder, A.; Nilam, R.; Rajendran, A.; Farooq, S.; Karimi, I. A.; Amanullah, M. Multiobjective optimization of a four-step adsorption process for postcombustion CO2 capture via finite volume simulation. *Ind. Eng. Chem. Res.* **2013**, *52*, 4249−4265.

(60) Glueckauf, E.; Coates, J. I. 241. Theory of chromatography. Part IV. The influence of incomplete equilibrium on the front boundary of chromatograms and on the effectiveness of separation. *J. Chem. Soc.* **1947**, 1315−1321.

(61) Zhu, X.; Ge, T.; Yang, F.; Wang, R. Design of steam-assisted temperature vacuum-swing adsorption processes for efficient CO2 capture from ambient air. *Renewable Sustainable Energy Rev.* **2021**, *137*, No. 110651.

(62) Wilkins, N. S.; Rajendran, A.; Farooq, S. Dynamic column breakAnnu. Rev. Chem. Biomol. Eng.ments for measurement of adsorption equilibrium and kinetics. *Adsorption* **2021**, *27*, 397−422.

(63) Krishnamurthy, S.; Lind, A.; Bouzga, A.; Pierchala, J.; Blom, R. Post combustion carbon capture with supported amine sorbents: From adsorbent characterization to process simulation and optimization. *Chem. Eng. J.* **2021**, *406*, No. 127121.

(64) Thakkar, H.; Eastman, S.; Al-Mamoori, A.; Hajari, A.; Rownaghi, A. A.; Rezaei, F. Formulation of Aminosilica Adsorbents into 3D-Printed Monoliths and Evaluation of Their CO2 Capture Performance. *ACS Appl. Mater. Interfaces* **2017**, *9*, 7489−7498.

(65) Bedford, R. E.; Tsang, C.-H. M. Improved Alumina-Ceria Catalyst Washcoat, EuropeanPatent Office EP0475490B1, 1994.

(66) Deutz, S.; Bardow, A. Life-cycle assessment of an industrial direct air capture process based on temperature-vacuum swing adsorption. *Nat. Energy* **2021**, *6*, 203−213.

(67) Wilkins, N. S.; Sawada, J. A.; Rajendran, A. Steam adsorption equilibrium data at 110 C on an activated carbon, Lewatit VP OC 1065, and CALF-20 using a microscale dynamic column breakthrough apparatus. *J. Chem. Eng. Data* **2023**, *69*, 1781−1803.

(68) Patton, A.; Crittenden, B. D.; Perera, S. P. Use of the linear driving force approximation to guide the design of monolithic adsorbents. *Chem. Eng. Res. Des.* **2004**, *82*, 999−1009.